JOURNAL OF COMPUTATIONAL PHYSICS 52, 545–568 (1983)

Convergence of Stochastic Orbit Computations

I. DILBER, J. M. WALSH, AND J. DENAVIT*

Department of Mechanical and Nuclear Engineering, Northwestern University, Evanson, Illinois 60201

Received January 4, 1983

Numerical integrations of stochastic orbits generally fail to yield convergent values of the particle position and velocity at a given time. In what sense do such computations remain valid? It is shown that numerical integrations accurately predict the global topography of stochastic orbits over long times compared to the field period. In numerical solutions of the Vlasov equation, no single particle is followed long enough to become stochastic. Do such solutions yield stochastic diffusion? This question is examined by comparing computations involving averages over a large number of stochastic particles with numerical solutions of the Vlasov equation.

I. INTRODUCTION

The motions of particles, under the action of deterministic fields, may in certain cases become unpredictable and acquire a "chaotic" or "stochastic" character [1, 2]. For example, two stochastic particles, which are initially infinitesimally close to each other in phase space, diverge from each other at an exponential rate, γ_{KS}, called "Kolmogorov–Sinai entropy" [2]. This irreversible behavior, in apparent violation of the deterministic laws of mechanics, causes diffusive effects, which are important in the evolution of plasmas confined by magnetic field, of interest in fusion applications or space plasma studies.

In particle simulation studies, numerical integrations of stochastic orbits do not converge in the usual sense. As shown in the examples of Section II, when the time step, Δt, approaches zero, the particle position in phase space after a finite time $t \gg \gamma_{KS}^{-1}$ does not approach any limit, but changes erratically with each change in the time step. This erratic behavior is the result of amplifications of round-off and truncation errors by many orders of magnitude by the Kolmogorov–Sinai entropy. In this paper we refer to errors occurring as a result of the finite number of significant figures retained in the computations as round-off errors, while truncation errors will denote the inaccuracies due to the finite time steps, Δt, used in numerical integrations.

Since stochastic orbit computations do not converge in detail, the validity of particle simulations involving stochastic orbits must rely on more global numerical convergence concepts. While a deterministic orbit may be represented as a one-

* Now at Lawrence Livermore National Laboratory.

0021-9991/83 $3.00

dimensional line in phase space, a stochastic orbit tends to fill out an entire region, with the particle visiting every part of the region if sufficient time is allowed. Thus, in the case of a stochastic orbit, numerical convergence must be based on the accuracy of this region, including its boundaries, rather than on the accuracy of the individual points themselves.

The purpose of the present paper is to develop this concept of numerical convergence of stochastic orbit computation, in terms of a simple one-dimensional case, and to test the performance of two algorithms on this problem: (i) the leap frog (LF) algorithm and (ii) the long-time-scale (LTS) algorithm [3]. The organization of the paper is as follows. The remainder of this introduction presents a brief review of basic concepts and notations necessary for an understanding of stochastic orbits. The detailed convergence of orbit computations is examined in Section II for both algorithms considered, and the difficulties preventing the convergence of stochastic orbits are discussed. Section III presents a series of computations showing how global convergence of stochastic orbits may be interpreted. Diffusion due to orbit stochasticity is studied in Section IV. The evolution of the distribution function of particles in phase space is considered by (i) the computation of orbits of a large number of particles, as in particle simulations and (ii) finite-element solutions of the Vlasov equation [4]. Comparison of the two approaches shows that solutions of the Vlasov equation, which do not involve directly the orbits of individual particles, nevertheless display the same diffusive effects of stochastic orbits as particle simulations. The main conclusions of the present study and their implication in particle simulation of plasmas are discussed in Section V.

Basic Concepts and Notations

Consider the motions of electrons in a one-dimensional external electric field of the form

$$E(x, t) = \sum_{m=-M}^{+M} A_m \sin(kx - m\,\Delta\omega t + \alpha_m) \tag{1}$$

consisting of the sum of $2M + 1$ mode, all having the same wavelength $L = 2\pi/k$, and having a discrete frequency spectrum with equally spaced frequencies, $\omega_m = m\,\Delta\omega$. The mode amplitudes, A_m, and phases, α_m, are constant. In the present paper the self-consistent field of the electrons is excluded, the electrons being treated as test particles to examine stochastic effects related to single-particle orbits. The electric field defined by Eq. (1) has a period $T = 2\pi/\Delta\omega$ and has $2M + 1$ equally spaced phase velocities $v_m = m\,\Delta\omega/k$, which are the velocities of resonant electrons. Under the action of a single mode, m, an electron may undergo either trapped or untrapped motion, depending on its initial conditions. The trapped-electron region in phase space is defined by $|v'| < V_m \cos[(kx' + \alpha_m)/2]$, as illustrated in Fig. 1, where $x' = x - v_m t$ and $v' = v - v_m$ are the electron position and velocity relative to the coordinate system moving with the phase velocity of mode m, $V_m = 2\Omega_m/k$ is the mode trapping velocity, $\Omega_m = (eA_m k/m_e)^{1/2}$ is the mode trapping frequence, $-e$ is the electron charge and m_e is the electron mass.

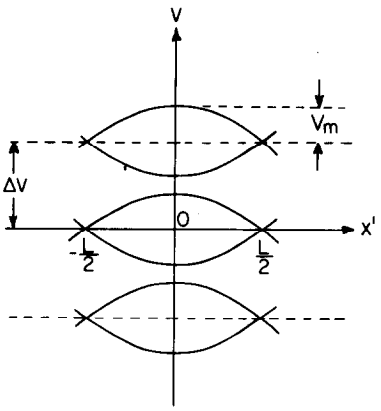

FIG. 1. Phase velocities and trapped-electron regions in phase plane.

The existence of stochastic orbits in the present problem depends on the mode amplitudes and is closely related to the overlap of adjacent trapping regions. For the equal amplitudes case, $A_m = A$, of primary interest because of simplicity, overlap occurs for $V_m \geqslant \Delta\omega/2k$, or for amplitudes $A > A_c$, where the critical amplitude, A_c, satisfies the relation $eA_c/m_e = \pi L/8T^2$. Normalized units are used in this paper, with lengths measured in units of the wavelent L, and A_m measured in units of the critical amplitude A_c. This defines the time unit through the overlap condition, such that $T^2 = \pi/8$. It follows that the normalized period is $T = \sqrt{\pi/8} \simeq 0.63$ and the normalized velocity increment between resonances is $\Delta v = 1/T \simeq 1.6$.

A special case occurs when an infinite number of modes is considered, with equal amplitudes, $A_m = A$, and zero initial phases $\alpha_m = 0$. In this case, Eq. (1) yields an impulsive electric field of the form

$$E(x, t) = A \sin 2\pi x \sum_{n=-\infty}^{\infty} \delta(t - nT). \tag{2}$$

Integrating the equations of motions of electrons under this electric field yields

$$\begin{aligned} v_{n+1} &= v_n - AT \sin 2\pi x_n, \\ x_{n+1} &= x_n + Tv_{n+1}, \end{aligned} \tag{3}$$

where x_n and v_n denote the electron position and velocity at time $t_n = nT - \varepsilon$ with $\varepsilon \to 0$, just prior to the application of an impulse. For this special case, the exact electron orbits depend on a set of finite-difference equations, Eqs. (3), which is called the "standard mapping" [2]. A number of analytical and numerical studies of stochastic orbits have been made in terms of finite-difference models of this type, rather than with the more realistic electric fields defined in Eq. (1) with a finite number of modes and arbitrary amplitudes and initial phases [5, 6].

The properties of the orbits defined by Eqs. (3) may be studied on the phase-plane

rectangle $0 \leqslant \bar{x} < 1$, $0 < \bar{v} \leqslant \Delta v$ by reducing the positions and velocities of the particles through the operations $\bar{x} = (x)_{\mathrm{mod}\,1}$, $\bar{v} = (v)_{\mathrm{mod}\,\Delta v}$ [5]. Here $(z)_{\mathrm{mod}\,a} = z - ai$, where i denotes the integer part of the ratio z/a. If x advances a distance R in Q steps, then the "winding number" is defined as $q = Q/R$. A "fixed point" of order Q is defined as a point which returns to its initial reduced position and velocity after Q steps, i.e., $\bar{x}_{n+Q} = x_n$ and $\bar{v}_{n+Q} = v_n$. First-, second- and third-order fixed points are illustrated in Fig. 2. A "tangent mapping" considers the evolution of the vector between two infinitesimally close points, $(\delta x, \delta v)$, given by differentiating Eqs. (3),

$$\begin{bmatrix} \delta v_{n+1} \\ \delta x_{n+1} \end{bmatrix} = M_n \begin{bmatrix} \delta v_n \\ \delta x_n \end{bmatrix}, \tag{4}$$

where

$$M_n = \begin{bmatrix} 1 & k_n/T \\ T & 1 + k_n \end{bmatrix}$$

and $k_n = -2\pi A T^2 \cos 2\pi x$. The eigenvalues $\lambda_n^{\pm}$ of the matrix M_n are given by

$$\lambda_n^{\pm} = 1 + \frac{k_n}{2} \pm \left[k_n \left(1 + \frac{k_n}{4} \right) \right]^{1/2}. \tag{5}$$

For $-4 < k_n < 0$, $|\lambda_n^{\pm}| = 1$ and the distance does not increase, but if this condition is not satisfied, $|\lambda_n^{+}| > 1$, the distance increases and, overlooking the dependence of k_n on x_n, one may define a growth rate $\gamma_{\mathrm{KS}} = (\ln |\lambda_n^{+}|)/T$, called "Kolmogorov–Sinai entropy" [1, 2]. Actually, the stability of a "fixed point" of order Q depends on the eigenvalues, $\lambda^{\pm}$, of the matrix [6]

$$M = \prod_{n=1}^{Q} M_n = \begin{bmatrix} \partial v_Q/\partial v_0 & \partial v_Q/\partial x_0 \\ \partial x_Q/\partial v_0 & \partial x_Q/\partial x_0 \end{bmatrix}. \tag{6}$$

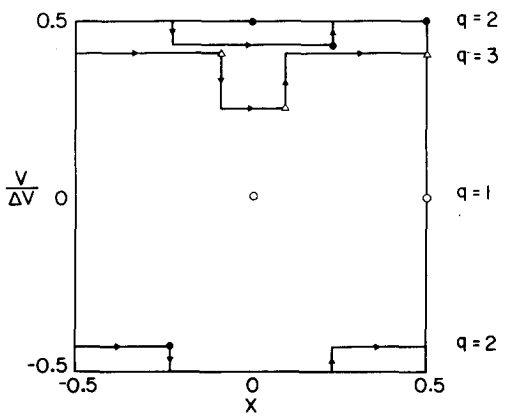

FIG. 2. Fixed points of the standard mapping.

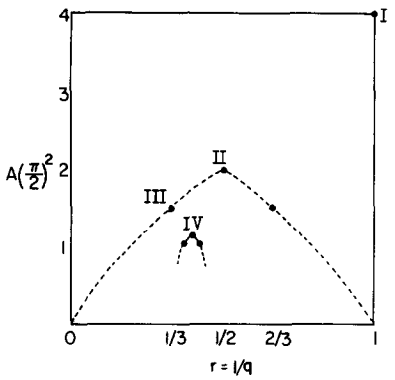

FIG. 3. Fractal diagram relating stability islands to the amplitude of the standard mapping.

Stability, which is characterized by $|\lambda^{\pm}| = 1$, requires $|\mathrm{Tr}\, M| < 2$, where $\mathrm{Tr}\, M$ denotes the trace of the matrix M. This criterion leads to the "fractal diagram" illustrated in Fig. 3 which gives maximum values of the amplitudes A for which the first-order fixed point (I), second-order fixed point (II), third-order fixed points (III), etc., are stable [7]. Each point lies at the center of stability island in the phase rectangle. A point initially within an island remains within the island, and has a deterministic orbit, while a point initialized outside any island has a stochastic orbit. As the amplitude is increased, the number of islands decreases, until for $A = (4/\pi)^2$ the largest island (I) disappears and only stochastic orbits generally remain.

However, even for large amplitudes ($A \to \infty$), the standard mapping still yields "islets of stability" for particular values of A satisfying the conditions [2]

$$(\pi^2/4)\, A \sin 2\pi x = 2\pi j,$$
$$0 < A \cos 2\pi x < 16/\pi^2$$

TABLE I

Amplitude Intervals for Which Islets of Stability Occur in Standard Mapping

j	Interval
1	$2.55 \lesssim A \lesssim 3.02$
2	$5.09 \lesssim A \lesssim 5.34$
3	$7.64 \lesssim A \lesssim 7.81$
4	$10.18 \lesssim A \lesssim 10.31$
5	$12.73 \lesssim A \lesssim 12.84$
6	$15.28 \lesssim A \lesssim 15.36$
7	$17.83 \lesssim A \lesssim 17.90$

where j is an integer. These conditions imply

$$(2\pi j)^2 < (\pi/2)^4 A^2 < (2\pi j)^2 + 16. \tag{7}$$

For $A > 16/\pi^2 \simeq 1.62$, i.e., when all regular islands have disappeared, islets of stability occur for the values of A within the intervals listed in Table I. Note that islets of stability occur only for narrow amplitude intervals, but that the amplitude itself can be arbitrarily large.

II. Detailed Convergence of Orbit Computations

In the computations presented here, the trajectory of an electron in the electric field defined by Eq. (1), with a maximum mode number $M = 15$, equal amplitudes $A_m = A = \text{const.}$ and zero initial phases, $\alpha_m = 0$, is integrated in time using two integration schemes. The first scheme is the standard leap-frog (LF) algorithm, where the position x is defined at times $n\,\Delta t$, while the velocity v is defined at times $(n + 1/2)\,\Delta t$, where Δt denotes the time step and n is an integer. This scheme is time centered and is accurate to second order in Δt, but Δt must be sufficiently small to resolve the shortest period of oscillation, T/M. With $M = 15$, values of the time step ranging from $\Delta t = T/75$ down to $\Delta t = T/600$ have been considered. The second scheme is a long-time-scale (LTS) algorithm specifically designed to follow particle motions in an electric field having the mode structure defined by Eq. (1) [3]. In the LTS algorithm, the equations of motion are integrated analytically to first order in the electric field amplitudes

$$v(t') = v(t) - \sum_m A_m \int_t^{t'} \sin\{k_m[x(t) + (t'' - t)\,v(t)] + \beta_m(t) - (t'' - t)\,\omega_m(t)\}\,dt''.$$

In the present case, $k_m = k$ is independent of m, $\beta_m(t) = \alpha_m - m\,\Delta\omega t$ and $\omega_m = m\,\Delta\omega$. Setting $t' = t + \Delta t$ gives

$$v(t + \Delta t) = v(t) + \sum_m A_m \left[\cos\psi_m \left(\frac{\cos\theta_m - 1}{\theta_m}\right) - \sin\psi_m \left(\frac{\sin\theta_m}{\theta_m}\right)\right] \Delta t$$

and similarly,

$$x(t + \Delta t) = x(t) + v(t)\,\Delta t + \sum_m A_m \left[\cos\psi_m \left(\frac{\sin\theta_m - \theta_m}{\theta_m^2}\right) + \sin\psi_m \left(\frac{\cos\theta_m - 1}{\theta_m^2}\right)\right] \Delta t^2,$$

where $\theta_m = k_m(v - \omega_m/k_m)\,\Delta t$ and $\psi_m = \beta_m + k_m x(t)$.

The time step is no longer limited by $\omega_m\,\Delta t \ll 1$ as in the leap-frog method but is limited by the condition $\Omega\,\Delta t \ll 1$, where $\Omega = (2\pi A)^{1/2}$ is the trapping frequency.

Since $\Omega \simeq \Delta\omega$ for conditions near overlap, time steps ranging from $T/10$ down to $T/150$ have been considered.

With the parameters considered here ($M = 15$, $A_m = A = \text{Const.}$ and $\alpha_m = 0$), the electric field has a pulse-like structure and results approaching the application of the standard mapping should be obtained. The computations of this section were done with $A = 0.9(2/\pi)^2 \simeq 0.3648$. Application of the standard mapping, with this amplitude, yields the phase diagrams of Fig. 4, in which a point is plotted for the position and velocity of a single particle, at time intervals T. To obtain plots comparable to the results of the time integrations to be carried out later, the velocities plotted in Fig. 4 are $v_n - (1/2)AT \sin 2\pi x_n$, which correspond to the center of the pulses ($t = nT$) rather than just prior to the pulse ($t = nT - \varepsilon$) as in Eqs. (3). The diagram of Fig. 4a corresponds to a stochastic particle initialized at $x_0 = -0.45$, $v_0 = 0$ which visits all locations in a phase-space area, excluding a major island (type I in Fig. 3) and several minor islands (types II and III). These islands correspond to deterministic orbits, and with the aid of Fig. 4a, a deterministic particle with initial conditions $x_0 = -0.45625$ and $v_0 = -0.199$ has been selected for test computations.

The phase plot of another stochastic orbit, located in the lower region of the phase rectangle is shown in Fig. 4b. Note that the "curves" of Fig. 4b constitute a single orbit surrounding five separate stability islands. The phase plots of three separate stable trajectories are shown in Fig. 4c.

A. *Deterministic Trajectories* ($x_0 = -0.45625$, $v_0 = -0.199$)

The computations for this case are summarizedin Table II, which gives values of

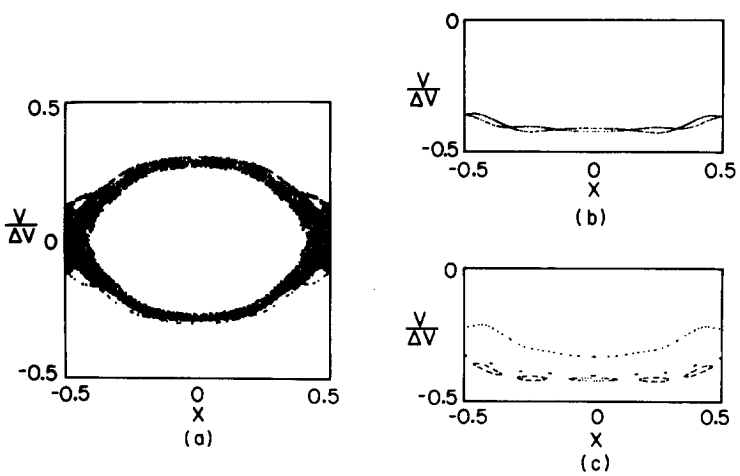

FIG. 4. Phase plots of the standard mapping for $A = 0.9(2/\pi)^2$. (a) Stochastic particle initialized at $x_0 = -0.45$, $v_0 = 0$ for $t = 5000T$; (b) stochastic particle initialized at $x_0 = 0.325$, $v_0 = -0.598$ for $t = 1000T$; (c) deterministic particles initialized at $x_0 = -0.175$, $v_0 = -0.598$; $x_0 = 0$, $v_0 = -0.638$; $x_0 = 0$, $v_0 = -0.654$ for $t = 200T$.

TABLE II

Final Positions x_f and Velocities v_f at $t = 200T$ from Deterministic Trajectory Computations, $x_0 = -0.45625$, $v_0 = -0.199$

LF			LTS		
Δt	$(x_f)_{\text{mod 1}}$	v_f	Δt	$(x_f)_{\text{mod 1}}$	v_f
$T/75$	−0.4503	−0.2080	$T/20$	−0.4522	−0.1927
$T/150$	−0.4511	−0.2001	$T/40$	−0.4461	−0.1976
$T/300$	−0.4512	−0.1965	$T/80$	−0.4499	−0.1936
$T/600$	−0.4523	−0.1947	$T/150$	−0.4509	−0.1930

the final position and velocity for both algorithms and various time steps. The phase plots for these computations are identical for all cases and only one typical plot is shown in Fig. 5. The phase points at intervals of T are all within a set of islands of the standard mapping, see Fig. 4. The final position and velocity at $t = 200T$ given in Table II, converge roughly toward the same values $(x_f)_{\text{mod 1}} \to -0.451$, $v_f \to -0.193$ for both algorithms as the time step is decreased.

For each case, the trajectory of a second particle initialized at $x_0' = x_0 + 10^{-10}$ $v_0' = v_0$, i.e., very close to the first particle was also computed. The distance between these particles, $d = [(x' - x)^2 + (v' - v)^2]^{1/2}$, was plotted as a function of time, and typical plots of this type for both algorithms are shown in solid line in Fig. 6. The distance between particles oscillates and grows only slightly over the duration of each run. This is expected for the deterministic trajectory considered here. A very different behavior will be found for the stochastic trajectory considered later.

Another test of accuracy is reversibility, i.e., restarting the computation with the particle in its final condition and moving backward in time. The reversed distance plots are shown in broken line in Fig. 6. For the leap-frog algorithm, which is time centered, perfect reversibility is obtained and the broken line does not show up. The LTS algorithm is not time centered and the distance plot is not exactly reversible.

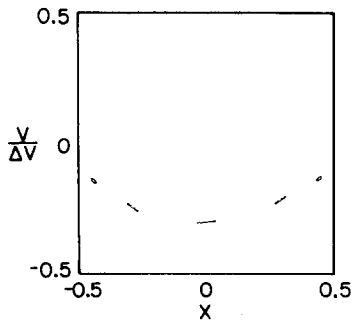

FIG. 5. Typical phase plot of a deterministic particle initialized at $x_0 = -0.45625$, $v_0 = -0.199$, from time integration with $A_m = 0.9(2/\pi)^2$, $\alpha_m = 0$, $m = 0, \pm 1, \ldots, \pm 15$.

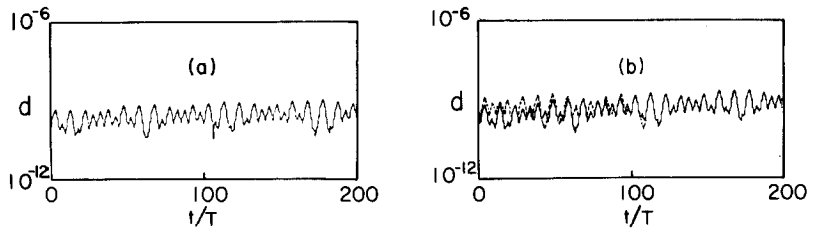

FIG. 6. Distance plots corresponding to the deterministic case of Fig. 5. Solid lines correspond to the forward computation and broken lines show the result of reversing the computation at $t = 200T$. (a) Leap frog algorithm with $\Delta t = T/150$. (b) LTS algorithm with $\Delta t = T/20$.

These results show that deterministic trajectory computations converge "in detail," in the sense that their accuracy could be expected to increase indefinitely as the time step Δt is decreased, and as the number of significant figures retained in the computations is increased.

B. *Stochastic Trajectory* ($x_0 = -0.45$; $v_0 = 0$)

The final positions and velocities of this particle at $200T$, using both algorithms, are given in Table III. These values do not converge to any limit as the time step is decreased. The final positions and velocities from the various computations listed in Table III are plotted in Fig. 7. These points are scattered over a region of the phase plane corresponding approximately to the stochastic region of the standard mapping (see Fig. 4), but none of the points enters the stability islands.

Typical distance plots for both algorithms are shown in solid line in Fig. 8. Note that the distance still oscillates, but now grows many orders of magnitude. During the first three oscillations, $t \lesssim 20T$, LF and LTS give identical results, but as the results of the two algorithms begin to diverge the detailed behavior varies. For $t \gtrsim 100T$ the distance approaches the size of the periodicity rectangle and cannot grow further.

These computations were reversed at $t = 100T$ (i.e., before the distance reaches the

TABLE III

Final Positions x_f and Velocities v_f at $t = 200T$ from Stochastic Trajectory Computations, $x_0 = -0.45$, $v_0 = 0$

LF			LTS		
Δt	$(x_f)_{\text{mod 1}}$	v_f	Δt	$(x_f)_{\text{mod 1}}$	v_f
$T/75$	−0.3628	0.1243	$T/10$	−0.6883	−0.3106
$T/150$	−0.0546	0.4213	$T/20$	0.4320	0.0836
$T/225$	−0.1774	−0.3976	$T/30$	0.4298	−0.0118
$T/300$	−0.3918	−0.2346	$T/40$	0.6443	−0.2208

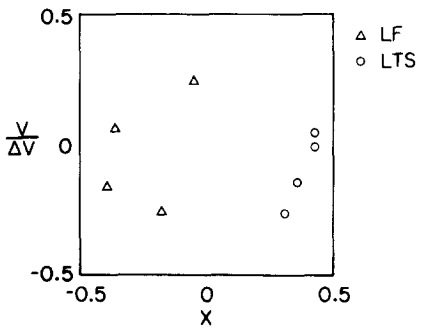

FIG. 7. Final positions in phase space of the stochastic particle obtained from computations listed in Table III.

size of the rectangle) and the results of the reverse runs are shown in broken line in Fig. 8. Leap frog (LF), which is time centered, gives the best reversibility but looses reversibility at $t \simeq 50T$. The reversed computations were initialized with 12 significant figures. Thus, after running from $t = 100T$ to $t = 50T$, the initial error of 10^{-12} has grown to $10^{-12} \times \exp[\gamma(100 - 50)T]$. Here, γ is the average growth rate of the distance during this period, which can be estimated at $\gamma \simeq 0.2/T$ from the forward distance plot in the same time interval. Thus the expected error of the reverse run at $t = 50T$ is $10^{12} \times \exp[0.2(100 - 50)] \simeq 10^{-8}$, which corresponds to the distance for which the forward and reverse runs become distinct in Fig. 8a. Therefore, the irreversibility of the LF computation is explained by the rapid amplification of the initial round-off error. For the LTS algorithm, which is not time centered, irreversibility results from the amplification of both truncation and round-off errors. For this algorithm, the reverse run becomes distinct from the forward run more rapidly (see Fig. 8b).

These example demonstrate that stochastic trajectory computations do not

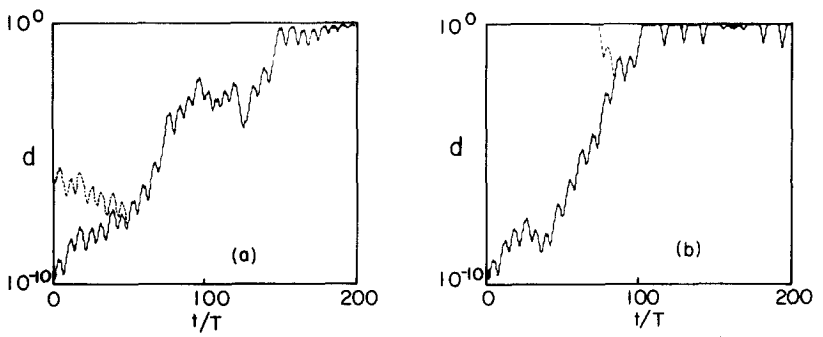

FIG. 8. Distance plots corresponding to a stochastic particle initialized at $x_0 = -0.45$, $v_0 = 0$ with the field amplitudes and phases corresponding to the case of Fig. 5. (a) Leap-frog algorithm with $\Delta t = T/150$; (b) LTS algorithm with $\Delta t = T/20$.

converge in the detailed sense applicable to deterministic trajectories. In the case of stochastic trajectories, truncation and round-off errors are rapidly amplified and dominate the results after a short time. However, the results of stochastic trajectory computations, although not completely predictable, are not random, and appear confined to the stochastic regions predicted by standard mapping computations. This question is examined in the following sections.

III. Global Convergence of Stochastic Orbit Computations

Some of the computations listed in Table III have been continued out to several thousand periods (3000T to 10000T) to observe the long-time behavior of stochastic trajectories. Recall that equal amplitudes, $A_m = A$, and zero initial phases, $\alpha_m = 0$, $m = 0, \pm 1, \ldots, \pm 15$ are considered, so that trajectories approaching the standard mapping trajectories should be obtained. The relatively low amplitude, $A = 0.9(2/\pi)^2 = 0.3648$, below the overlap value, gives a number of stochastic regions separated by KAM surfaces and including stability islands of various sizes as shown in Fig. 4. This configuration appears to be appropriate for accuracy tests.

Phase plots of the trajectory for $t = 5000T$, computed with the leap frog algorithm using $\Delta t = T/150$ and $T/300$ are shown in Fig. 9. These phase plots are in good agreement with the standard mapping phase plot, Fig. 4a, displaying the same overall topography, boundaries and details of the small islands. Thus, although the location of individual phase points differs in these plots, as demonstrated in Section II, the global pattern generated by these points is computed accurately.

Some differences are observed between Figs. 9a and b regarding the density of phase points. This is due to the different order in which the various parts of the stochastic region are visited in the two computations. Each computation using a different time step, or initialized at a slightly different point, covers the stochastic

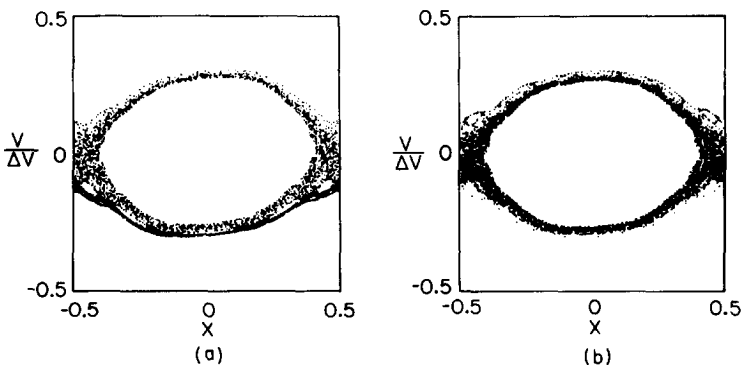

FIG. 9. Phase plots for $t = 5000T$ of a stochastic particle initialized at $x_0 = 0.45$, $v_0 = 0$ using the leap-frog (LF) algorithm (a) $\Delta t = T/150$; (b) $\Delta t = T/300$. Electric field with $A_m = 0.9(2/\pi)^2$, $\alpha_m = 0$, $m = 0, \pm 1, \ldots, \pm 15$.

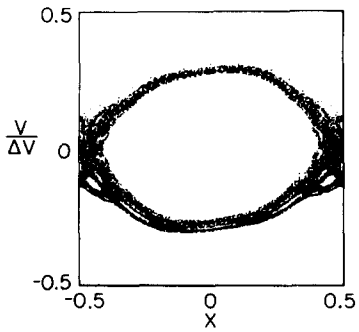

FIG. 10. Phase plot of the same particle and field as in Fig. 9 for $t = 10000T$, using leap frog with $\Delta t = T/150$.

region in a different way. The phase plot for $t = 10000T$, using $\Delta t = 1/150$, is shown in Fig. 10. Note that as more points are added, the phase plot acquires a more uniform density and its details become more clearly defined.

This example illustrates the concept of "global convergence" of the computation of a stochastic orbit: as the accuracy of the computation is increased and as more points are added to the phase plots by continuing the computation over longer times, the region covered by the trajectory becomes more sharply and accurately defined.

Phase plots of the trajectory for $t = 5000T$, using the LTS algorithm with $\Delta t = T/10$ and $\Delta t = T/20$ are shown in Fig. 11. While the computation with $\Delta t = T/20$, Fig. 11b, gives the correct pattern of points, in agreement with the previous results, the phase point with $\Delta t = T/10$, Fig. 11a, moves into the lower region of the rectangle giving a new pattern. Other computations with slightly different initialization yield a similar pattern in the upper region of the rectangle. The inaccuracies occurring in Fig. 11a may be understood by referring to the orbits obtained from the standard mapping by initializing particles below the stochastic

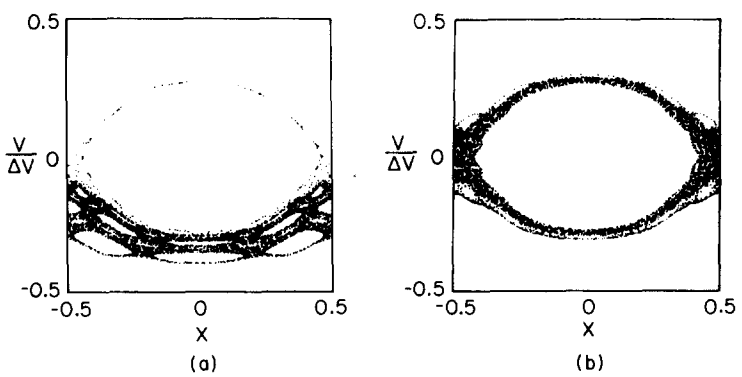

FIG. 11. Phase plots for $t = 5000T$ of the same particle and field as in Fig. 9, using the LTS

region of Fig. 4a. This lower region is occupied by narrow stochastic orbits surrounding stable islands as shown in Fig. 4b. However, these orbits are separate and a phase point initialized on one such orbit does not migrate to others. With $\Delta t = T/10$, the LTS algorithm is evidently not sufficiently accurate to always maintain the phase point on the same stochastic orbit. The phase point is allowed to jump from one stochastic orbit to another and to fill the entire region, but does not enter the stability islands.

Several additional computations were done to examine stable and stochastic orbits in the lower region of the phase rectangle when LF (with $\Delta t = T/150$) and LTS (with $\Delta t = T/20$) are used. The results of two stochastic cases are shown in Figs. 12a and b, using LF and LTS, respectively, and good agreement between the two methods is evident. Note that, although these trajectories are very narrow, they are indeed stochastic as demonstrated by their exponentiating distance plots (not shown here). Similarly, two stable cases with LF shown in Fig. 12c and LTS shown in Fig. 12d also give good agreement. These computations demonstrate that both LF and LTS can compute these orbits accurately and maintain them separated, provided that a sufficiently small time step is used.

As the amplitude is increased the stability islands of the standard mapping disappear and for $A > 4(2/\pi)^2$ the entire phase space rectangle is generally occupied by a single stochastic trajectory. However, for values of A lying in particular narrow intervals, small stability islets occur as discussed in Section I. Two stable standard mapping orbits lying within stability islets with $A = 6.6(2/\pi)^2$ are shown in Fig. 13a.

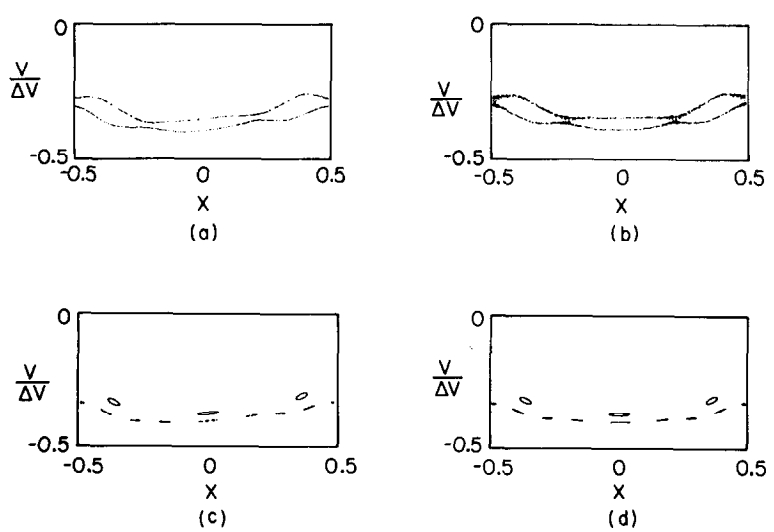

FIG. 12. (a) Phase plots of two stochastic particles in the lower region of the phase rectangle using the leap-frog algorithm with $\Delta t = T/150$ for the same field as in Fig. 9. (b) Same as (a) but using the LTS algorithm with $\Delta t = T/20$. (c) Phase plots of two deterministic particles in the lower region of the phase rectangles, using the leap-frog algorithm with $\Delta t = T/150$, for the same field as in Fig. 9. (d) Same as (c) but using the LTS algorithm with $\Delta t = T/20$.

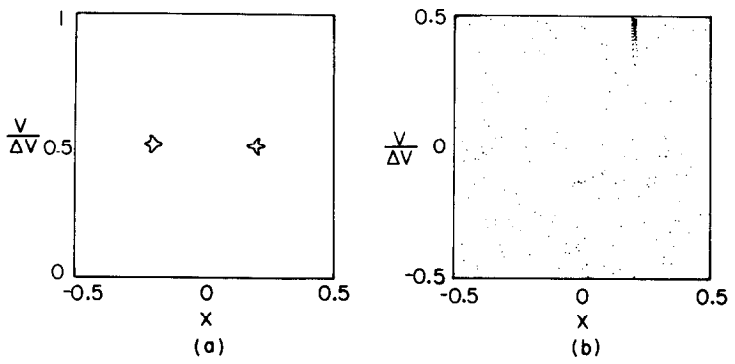

FIG. 13. (a) Two stable standard mapping orbits obtained by placing a particle inside each islet for $A = 6.6(2/\pi)^2$, $t = 500T$. (b) Phase plot of a particle initialized in the right islet for the LTS algorithm with $A = 6.6(2/\pi)^2$, $t = 200T$, $\Delta t = T/80$ and $m = 0, \pm 1, ..., \pm 50$. Note the particle drift in the $-v$ direction causing the particle to gradually leave the islet and to become stochastic (scattered points).

The question of the existence of islets in numerical integrations with a finite number of modes was examined with the LTS and leap-frog algorithms by initializing the particle inside the right islet of Fig. 13a. The results of such an integration for $t = 200T$, using LTS with $\Delta t = T/80$ and $m = 0, \pm 1, ..., \pm 50$, is shown in Fig. 13b. The particle remains stable within the islet for some time, but drifts slowly in the $-v$ direction. Ultimately, this drift causes the particle to leave the islet and become stochastic, generating scattered points all over the phase rectangle. This phase plot shows that the drift velocity increases with time, and distance plots (not given here) show oscillations which gradually increase in amplitude, until they become unbounded when transition to stochasticity occurs. Other computations show that the drift velocity increases as the number of mode is decreased. Similar results were obtained with the leap-frog algorithm, but in this case very small time steps, $\Delta t = T/600$, must be used to properly resolve the time dependence of the high-frequency modes. In summary, stability islets can, in principle, be recovered by time-integration methods. However, their existence is a particularity of the standard mapping, which can be recovered only in the limit of an infinite number of modes.

Having shown that time integration techniques (LF or LTS) can indeed generate the global properties of the standard mapping, with the possible exception of islets of stability, we may now use these techniques to compute stochastic trajectories resulting from more realistic electric fields involving arbitrary initial phases for example. The phase plot from such a computation, for $t = 5000T$, using LF is shown in Fig. 14a. The initial phases for this computation were taken from a random-number generator with uniform probability between 0 and 2π and are listed in Table IV. The amplitudes of all modes were $A = 0.9(2/\pi)^2$, the same value as in Figs. 9 thru 12. This phase plot displays the same topological features as the corresponding standard mapping plot, but it is somewhat distorted. Several computations with the same field amplitude and initial phases, but with different

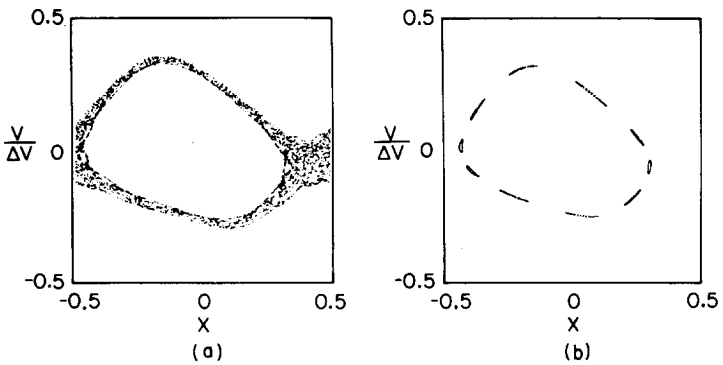

FIG. 14. Phase plots from time integration using leap frog with $\Delta t = T/150$, $A = 0.9(2/\pi)^2$, α_m listed in Table IV from a random number genertor and $m = 0, \pm 1, ..., \pm 15$. (a) Stochastic particle for $t = 3000T$. (b) Deterministic particle for $t = 1000T$.

initialization or a smaller time step, $\Delta t = T/300$, are in good agreement with the result of Fig. 14a. Finally, when the particle is initialized within one of the small islands of Fig. 14a, the stable orbit of Fig. 14b is obtained.

The computations carried out in this section have shown that, although time integration techniques applied to stochastic orbits do not yield numerically

TABLE IV

Initial Phases Used in Computations of Phase Plots of Fig. 14. (From Random-Number Generator)

m	α_m	m	α_m
−15	5.400	1	5.202
−14	5.301	2	3.319
−13	4.909	3	6.008
−12	6.185	4	4.863
−11	1.669	5	5.994
−10	5.890	6	4.406
−9	5.108	7	0.221
−8	1.267	8	6.241
−7	5.823	9	1.117
−6	1.668	10	3.990
−5	0.912	11	4.200
−4	3.177	12	0.250
−3	2.279	13	2.818
−2	1.033	14	5.293
−1	0.486	15	1.493
0	0.450		

convergent phase points at any particular time, the global pattern generated by such phase points over long times is numerically convergent, provided that sufficiently short time steps are used.

IV. Diffusion

The most important manifestation of orbit stochasticity is the occurrence of particle diffusion under the action of forces derived from deterministic fields [2]. In this section we consider the evolution of a large electron population in one dimension, defined by its density in phase $f(x, v, t)$. In addition to $f(x, v, t)$ we will be concerned with the "fine-grained" velocity distribution function,

$$F(v, t) = \frac{1}{L} \int_0^L f(x, v, t)\, dx, \tag{8}$$

which involves an averaging over the entire system, and "coarse-grained" velocity distribution functions,

$$\bar{F}(v, t) = \frac{1}{\eta} \int_{v-\eta/2}^{v+\eta/2} F(v', t)\, dv' \tag{9}$$

involving an additional local averaging with respect to velocity over the interval η.

We are concerned here with the evolution of the coarse-grained distribution functions when the density in phase is a solution of the Vlasov equation with specific initial condition,

$$\frac{\partial f}{\partial t} + v \frac{\partial f}{\partial x} - E \frac{\partial f}{\partial v} = 0, \tag{10}$$

where $E(x, t)$ is given by Eq. (1) and $f(x, v, t = 0)$ is specified. When the overlap condition is satisfied, this problem is expected to follow a diffusive model in which the coarse-grained distribution functions are governed by

$$\frac{\partial \bar{F}}{\partial t} = \frac{\partial}{\partial v} D(v) \frac{\partial \bar{F}}{\partial v}, \tag{11}$$

where the velocity diffusion coefficient $D(v)$ depends on the mode amplitudes A_m. In particular, if all mode amplitudes are equal, $A_m = A$, the diffusion coefficient is uniform, $D = C(A^2 - 1)$, where C is a constant, and Eq. (11) may be solved analytically. For example, in the interval $-v_b \leqslant v \leqslant v_b$, with boundary conditions $\bar{F}(\pm v_b, t) = 0$, the initial condition $\bar{F}(v, t = 0) = \cos(\pi v / 2v_b)$ yields

$$\bar{F}(v, t) = \exp\left[-\left(\frac{\pi}{2v_b} \right)^2 Dt \right] \cos\left(\frac{\pi v}{2v_b} \right). \tag{12}$$

Thus the coarse-grained distribution retains a cosine distribution between the boundaries at $\pm v_b$, but its amplitude decreases exponentially with time. The number of particles, $N = \int_{-v_b}^{+v_b} \bar{F}(v, t)\, dv$ and the kinetic energy, $W = \int_{-v_b}^{+v_b} v^2 \bar{F}(v, t)\, dv$ have initial values $N_i = 4v_b/\pi$, $W_i = (\pi^2/2 - 4)(2v_b/\pi)^3$ and decay in time according to the exponential in Eq. (12). Physically, particles diffuse and are "absorbed" as they reach the velocity boundaries.

The preceding example will be used to test and compare two methods to compute the diffusive effects of stochastic particles. In the first method, the trajectories of a large number of particles are computed, from which the density in phase and the resulting coarse-grained distribution function are evaluated. In the second method, the Vlasov equation is solved by finite-element methods in the phase plane (x, v), after which velocity distribution functions are evaluated. The LTS time integration method will be used in both methods because of its greater numerical efficiency than leap frog for this application.

A. *Particle Orbit Method*

The phase space in the interval $-v_b \leqslant v \leqslant v_b$ is covered with a rectangular grid as shown in Fig. 15a, representing the locations of phase points at some *final* time t_f. The value of the distribution function at each point is obtained by integrating the orbit *backward* in time to x_0, v_0 at $t = 0$ and applying the principle of constant density in phase along a phase-space trajectory,

$$f(x, v, t_f) = f(x_0, v_0, t = 0), \tag{13}$$

which is equivalent to the Vlasov equation. The initial density in phase is $f(x_0, v_0, t = 0) = \cos(\pi v_0/2v_b)$ for particles which never reach the boundaries at $\pm v_b$, and the boundary conditions are maintained by setting $f(x, v, t_f) = 0$ for a particle reaching either boundary at $\pm v_b$ for any time $t < t_f$ during its backward journey in

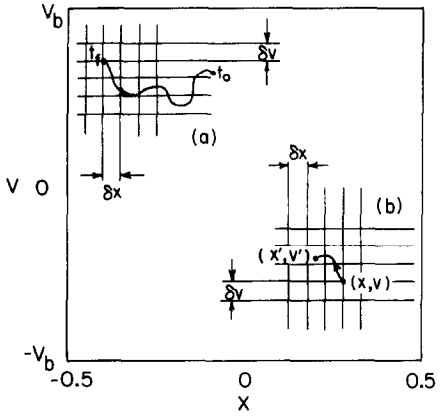

FIG. 15. (a) Computation grid used to evaluate the density in phase by particle orbit method. (b) Computation grid used in numerical integrations of the Vlasov equation.

time. This method provides values of the density in phase at uniformly spaced grid points within the region of interest. It avoids all numerical averaging in phase space, leaving only time integration and round-off errors as sources of inaccuracies. However, it provides results at one time only. Since backward integration in time is involved, values of f over the grid at a time $t < t_f$ would require a new evaluation of the orbits.

A series of computations was carried out with equal amplitudes $A_m = A$, final phases $\alpha_m(t_f) = m\,\Delta\omega t_f$ corresponding to zero initial phases and $m = 0, \pm 1, \ldots, \pm 15$. The fine-grained distribution and two coarse-grained distributions at $t = 50T$ and for $A = 1.5$, corresponding to overlapping trapping regions with $v_b = 5.5\Delta v$, are shown in Fig. 16. The initial distribution function is shown in broken line in these plots. Note the noisy nature of the fine-grained distribution. The coarse-grained distributions have an approximate cosine distribution, as predicted by the diffusion model, Eq. (11), but also have a fine structure closely related to the resonant velocities of the individual modes. Values of the diffusion coefficient may be obtained by computing the number of particles and the kinetic energy at the final time, $N_f = \int_{-v_b}^{+v_b} F(v, t_f)\,dv = 8.80$, and $W_f = \int_{-v_b}^{+v_b} v^2 F(v, t_f)\,dv = 118.6$, and equating the ratios N_f/N_i and W_f/W_i to the exponential in Eq. (12). This procedures gives two diffusion coefficients, D_N and D_E, based on the number of particles and on the kinetic energy, respectively. The values of these coefficients are listed in Tables V and VI, together with similar values obtained using different time steps and field amplitudes.

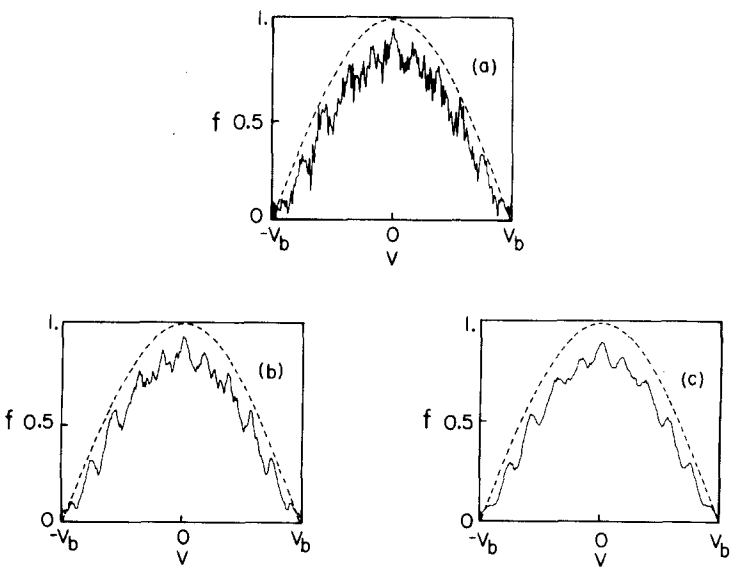

FIG. 16. Fine-grained and coarse-grained distribution functions for $A = 1.5$ at $t = 50T$, using the particle orbit method. (a) fine grained; (b) coarse grained, averaged over three velocity grid points; (c) coarse grained, averaged over seven velocity grid points.

TABLE V

Density and Energy Diffusion Coefficients, D_N and D_E, from Particle Orbit Method. Dependence on Numerical Parameter, with $A = 1.5$ and $\delta v = 2v_b/(k_{max} - 1)$

Δt	k_{max}	D_N	D_E
$T/16$	471	0.23	0.31
$T/16$	235	0.24	0.33
$T/32$	471	0.22	0.26

B. *Solutions of the Vlasov Equation*

A rectangular grid covering a phase plane region in the interval $-v_b \leqslant v \leqslant v_b$, as illustrated in Fig. 15b, is also used here, but weighted particles are now assigned at each grid point according to the local value of the distribution function at a particular time, t. Each particle is advanced forward over a single time step Δt, for example from (x, v) to (x', v') in Fig. 15b, after which the distribution function is reconstructed at $t' = t + \Delta t$ [4]. The boundary conditions $f(x, \pm v_b, t) = 0$ are enforced by setting appropriate values of two rows of guard cells above and below the boundaries at $\pm v_b$. This method is also based on conservation of density in phase along particle trajectories, $f(x', v', t') = f(x, v, t)$, but now applied only over short time intervals Δt. Redistribution of the particle weights at each time step is done in a manner which conserve first- and second-order moments, but involves repeated averaging operations, instead of the single averaging carried out in the preceding method. This introduces space and velocity grid errors which must be added to time integration errors, and it is not evident that stochastic particle effects are correctly represented by this method.

A series of solutions, listed in Table VII, were done with equal amplitudes $A_m = A = 1.5$, zero initial phases $\alpha_m = 0$, $m = 0, \pm 1, ..., \pm 15$, and $v_b = 5.5\Delta v$. The velocity

TABLE VI

Density and Energy Diffusion Coefficients, D_N and D_E, from Particle Orbit Method. Dependence on Amplitude, with $k_{max} = 471$ and $\Delta t = T/16$

A	D_N	D_E
0.5	0.007	0.01
1.0	0.07	0.12
1.5	0.23	0.31
2.0	0.56	0.59

TABLE VII

Density and Energy Diffusion Coefficiens, D_N and D_E, from Vlasov Solution. Dependence on Numerical Parameters, with $A = 1.5$ and $\delta v = 2v_b/(k_{max} - 1)$

Δt	k_{max}	D_N	D_E
$0.1/\sqrt{2\pi}$	471	0.22	0.24
$0.1/\sqrt{2\pi}$	235	0.23	0.26
$0.05/\sqrt{2\pi}$	471	0.21	0.25

distribution, $F(v, t)$ at $t = 50T$ for two values of the time step Δt and of the velocity mesh size δv are given in Fig. 17. The initial distribution function is shown in broken line in these plots. These plots are in good agreement with each other and with the coarse-grained results of the particle orbit method described earlier. Plots of the number of particles and of the kinetic energy as a function of time are given in Fig. 18, and the corresponding values of D_N and D_E are listed in Table VII. These values are consistent with each other and are also in general agreement with the result of the particle orbit method. Note, however, that somewhat larger diffusion rates are

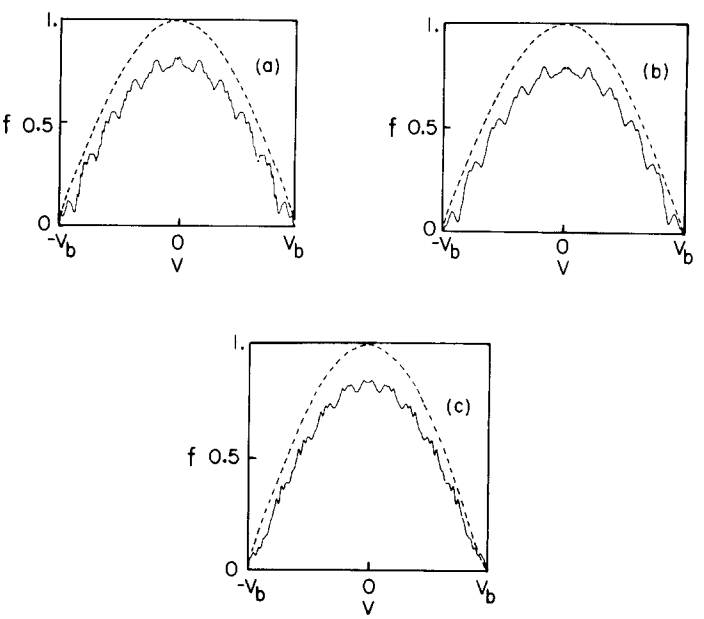

FIG. 17. Distribution functions normalized to initial maximum for $A = 1.5$ at $t = 50T$, using Vlasov solutions. (a) $\Delta t = 0.1/\sqrt{2\pi}$, $\delta v = v_b/235$. (b) $\Delta t = 0.1/\sqrt{2\pi}$, $\delta v = v_b/117$. (c) $\Delta t = 0.05/\sqrt{2\pi}$, $\delta v = v_b/235$.

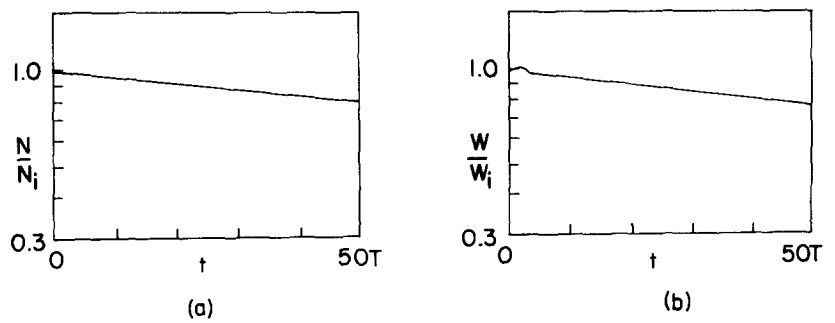

FIG. 18. Number of particles and kinetic energy vs. time from the Vlasov solution with $A = 1.5$, $\Delta t = 0.1/\sqrt{2\pi}$, $\delta v = v_b/235$.

obtained for the largest mesh size and smaller time step. This is interpreted as the result of numerical diffusion superimposed over the stochastic diffusion rate.

For the quadratic reconstruction scheme used in the present computations, the numerical diffusion is given by

$$D_{\text{num}} = \left(\frac{2v_b}{\pi}\right)^2 \frac{D^{(2)}(q)}{\Delta t},$$

where $D^{(2)}(q)$ is the normalized diffusion at each time step, which was estimated in Ref. [4] as a function of the velocity mode $q = 2\pi/\Delta v$ and of the grid spacing $\delta v = 2v_b/(k_{\max} - 1)$. For $v_b = 5.5\Delta v$ and $k_{\max} = 235$, $q\,\delta v/\pi \simeq 0.1$ from which (see Table I of Ref. [4]) $D^{(2)}(q) = 2 \times 10^{-4}$. For $\Delta t = 0.1/\sqrt{2\pi}$, the numerical diffusion rate is $D_{\text{num}} = 0.016$. For small values of $q\,\delta v/\pi \ll 1$, $D^{(2)}(q)$ scales as q^3; whence for $k_{\max} = 471$ the numerical diffusion rate is reduced to $D_{\text{num}} \simeq 0.002$. These values explain the reduction in both D_N and D_E observed in Table VII when k_{max} is increased from 235 to 471 with $\Delta t = 0.1/\sqrt{2\pi}$. With $\Delta t = 0.05/\sqrt{2\pi}$ and $k_{\max} = 471$ the numerical diffusion estimate is $D_{\text{num}} \simeq 0.004$, which explains the value $D_E = 0.25$, somewhat larger than for $\Delta t = 0.1/\sqrt{2\pi}$, but does not explain the lower value of D_N.

TABLE VIII

Density and Energy Diffusion Coefficients, D_N and D_E, from Vlasov Solution. Dependence on Amplitude, with $k_{\max} = 471$ and $\Delta t = 0.1/\sqrt{2\pi}$

A	D_N	D_E
0.5	0.002	−0.01
1.0	0.06	0.08
1.5	0.22	0.24
2.0	0.58	0.59

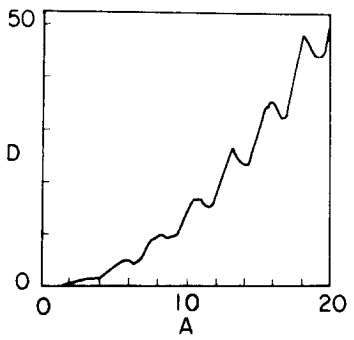

FIG. 19. Diffusion coefficient as a function of amplitude, A, for standard mapping.

Finally, several amplitudes, A, were considered and the corresponding values of the stochastic diffusion coefficients D_N and D_E are given in Table VIII.

The results of these computations show that Vlasov solutions accurately represent the diffusive effect of stochastic particle motion, provided that sufficiently small mesh sizes are used to prevent the occurrence of additional numerical diffusion.

The particle orbit method was also applied to the standard mapping [8], and the diffusion coefficient for this case has the amplitude dependence shown in Fig. 19. To obtain accurate results over a wide range of values of A, the velocity boundaries at $\pm v_b$ were chosen for each value of A to maintain a constant value of the ratio $R = v_b/AT$, and the discrepancy between D_N and D_E was negligible. This plot, and similar results using values of R ranging from 3.5 to 11, show that the average value of D follows the scaling law $D_{\text{avr}} = C(A^2 - 1)$, where $C = 0.135 \pm 0.02$. This values is consistent with the diffusion coefficients of Tables VI and VIII, but the results of these tables were not carried to sufficiently large amplitudes to allow an accurate comparison. The dependence of D on A in Fig. 19 also oscillates with period $\Delta A \simeq 2.5$. These anomalous oscillations were found independently, but they had been discovered earlier [9]. They are related to the existence of stability islets of the standard mapping, which occur for amplitudes corresponding to the relative maxima of the diffusion coefficient (see Table I).

V. CONCLUSIONS

Time integration methods applied to stochastic particle trajectories fail to yield numerically convergent values of the position and velocity of an individual particle at a particular time. This loss of accuracy is the result of rapid amplification of truncation and round-off errors by the K–S entropy. For some problems, such as the determination of a spacecraft trajectory under the influence of complex gravitational fields, for example, this failure of numerical integration methods would cause serious difficulties. However, in plasma physics applications, the state of an individual

particle at a particular time is not usually of interet. The quantities of interest are either time averages of an individual particle motion, or aggregate averages at a particular time over a large number of particles. The real test of integration schemes therefore depends on the numerical convergence of these global properties, rather than on the convergence of the detailed motion of individual particles. These global convergence questions have been examined in the context of one-dimensional motion of electrons in an electric field consisting of a sum of modes defined by Eq. (1). The long-time convergence of the trajectory of an individual stochastic electron has been considered in terms of phase plots in Section III, and the convergence of averages over a large number of electrons has been considered in terms of diffusion in Section IV. In both cases it was found that numerical integration schemes yield accurate results, provided that sufficiently small time steps are used.

The computations of Section IV show that numerical solutions of the Vlasov equation, which deal directly with the evolution of the particle distribution function in an apparently deterministic manner, yield the same stochastic diffusion results as methods based on actual computations of stochastic orbits.

Over long times ($t \gg T$) solutions of the Vlasov equation tend to acquire fine-grained structures, which result from the fact that two neighbouring phase points at a given time t originate from distant initial conditions at $t = 0$. Although each time step with $\Delta t \lesssim T$ is deterministic, the distribution function retains a long "memory" of the initial conditions. Small perturbations in the distribution function are therefore subject to the same type of K–S entropy as the intidividual stochastic orbits on which it depends locally. If numerical diffusion could be excluded entirely, Vlasov solutions would be different from computations based directly on particle orbits only in the manner in which the data are stored at each time step, $f(x, v, t)$ instead of $x(t)$ and $v(t)$. Thus identical results should be expected. The computations of Section IV provide proof that this agreement actually occurs within deviation which can be attributed to numerical diffusion.

ACKNOWLEDGMENTS

The authors wish to thank Marvin B. Lewis for informative discussions of fundamental problems of orbit stochasticity. This research was sponsored in part by the U.S. Department of Energy under Contracts DE-AC02-76ET53041 to Northwestern University and W-7405-ENG-48 to the Lawrence Livermore National Laboratory, and by the Office of Naval Research under Contract N00014-75-0473 to Northwestern University. Acknowledgment is made to the National Magnetic Fusion Energy Computing Center for computer times used in this research.

REFERENCES

1. R. G. H. HELLMAN, "Fundamental Problems in Statistical Mechanics" (E. G. D. Cohen, Ed.), Vol. 5, pp. 165–233, North-Holland, Amsterdam/New York, 1980.
2. B. V. CHIRIKOV, *Phys. Rep.* **15** (1979), 264.

3. C. E. RATHMANN, J. L. VOMVORIDIS, AND J. DENAVIT, *J. Comp. Phys.* **26** (1978), 408.
4. J. DENAVIT, *J. Comp. Phys.* **9** (1972), 75.
5. G. SCHMIDT, *Phys. Rev. A* **22** (1980), 2849.
6. J. M. GREENE, *J. Math. Phys.* **20** (1979), 1183.
7. G. SCHMIDT AND J. BIALEK, *Bull. Amer. Phys. Soc.* **26** (1981), 1012.
8. J. M. WALSH, "Particle Diffusion Due to Stochastic Orbits," M. S. Report, Department of Mechanical and Nuclear Engineering, Northwestern University, July 1981.
9. A. B. RECHESTER AND R. B. WHITE, *Phys. Rev. Lett.* **44** (1980), 1586.